

Multicolor Quantum Dots-in-a-Well Focal Plane Arrays

Thomas E. Vandervelde, Michael C. Lenz, Eric Varley, Ajit Barve, Jiayi Shao, Rajeev Shenoi, David A. Ramirez, Wooyong Jang, Yagya D. Sharma, and Sanjay Krishna*
Center for High Technology Materials at The University of New Mexico, 1313 Goddard St. SE,
Albuquerque, NM 87106 USA.

ABSTRACT

This paper discusses recent and future advancements in the field of quantum dots-in-a-well (DWELL) focal plane arrays (FPAs). Additionally, for clarity sake, the fundamentals of FPA figures of merit are reviewed. The DWELL detector represents a hybrid between a conventional quantum well photodetector (QWIP) and a quantum dot (QD) photodetector (QDIP). This hybridization, where the active region consists of QDs embedded in a quantum well (QW), grants DWELLs many of the advantages of its components. This includes normally incident photon sensitivity without gratings or optocouplers, like QDIPs, and reproducible control over operating wavelength through ‘dial-in recipes’ as seen in QWIPs. Conclusions, drawn by the long carrier lifetimes observed in DWELL heterostructures using femtosecond spectroscopy, have recently backed up by reports of high temperature operation results for DWELL FPAs. This paper will conclude with a preview of some upcoming advances in the field of DWELL focal plane arrays.

Keywords: Photodetectors, Quantum Dots, Focal Plane Array, III-V, Semiconductors, and Infrared Detectors

1. INTRODUCTION

Due to the wide range of applications, the infrared portion of the electromagnetic spectrum has long been of interest for both military and civilian uses. The 3–25 μm infrared regime is of particular interest, this is due to its wide range of applications including: missile detection and tracking, battlefield imaging and communications, medical diagnostics and treatment, surveillance, and biological/chemical agent identification. Over the past ten to fifteen years, there has been significant interest in developing intersubband quantum dot (QD) infrared detectors (QDIPs) for the mid-(MWIR) and long-wave infrared (LWIR) regimes^[1–9]. The QDIP’s ability to collect normally incident photons, without the use of a grating or other optocoupler, and its potential for low dark currents is the primary reason for this interest. Presently, mercury–cadmium–telluride (MCT) detectors continue to demonstrate superior responsivity and specific-detectivity (D^*) when compared to the state of the art QDIPs or quantum well infrared photodetectors (QWIPs). Despite their superior performance, difficulties in spatial uniformity, epitaxial difficulties, and low fabrication yields make the manufacture of large FPAs exceedingly expensive^[10, 11]. This fact drives scientists and engineers to try to make intersubband systems competitive.

The utilization of quantum mechanical confinement of the charge carriers is one of the key factors in the performance of the intersubband detectors. This confinement enables the possibility of novel high performing devices^[12 & 13]. Standard QWIP heterostructures are based on the mature (In,Ga,Al)As materials system which increases the feasibility of industrial production of low cost, large scale, optoelectronic devices. Since many other optoelectronic devices are GaAs-based this also implies easy integration with other existing devices and circuits^[14]. The QDIPs, on the other hand, operate on both the bound-to-bound and B-C carrier transition within the QD and are measured as photocurrent. QDIPs have a number of advantages compared to QWIPs; specifically, they are sensitive to normally incident light. This sensitivity to normal photons originates in having the direction of quantum confinement parallel to the electric field of the incident photon. The confinement in QWIPs lies only in the growth direction; therefore, additional efforts must come into play to alter the trajectory on the incident light. QDs are zero-dimensional objects and, therefore, have confinement in three-dimensions^[10]. This implies that QDIPs are sensitive to light incident from any direction, including normal. Additionally, QDIPs have higher optical gain and carrier lifetimes are longer; therefore, the efficacy of a carrier providing photocurrent is greater for a QDIP than a QWIP^[15–18], which in turn could result in a significantly larger D^* ^[19]. Unfortunately, QDIPs also come with some serious drawbacks, specifically QDIPs have been experimentally shown to have high dark current values^[20–24]. It is believed, however, that these high dark current levels are largely due to dot formation issues and problems with subsequent overgrowth degrading the confinement. With

lower dark current levels predicted with better three-dimensional confinement of carriers, higher operating temperatures can also be expected, thereby reducing the complexity of associated cryo-coolers. QD detectors with a room temperature operation have already been demonstrated ^[25], and several other groups have shown some promising results in this spectral window ^[1-9], however, because of the intricate dependence of the operating wavelength on the size and shape of the dot, which in turn depends on the inherently random self-assembly process, presently there are no ‘dial-in recipes’ for obtaining a desired spectral response from QD detectors.

Our research group, as well as several others, are investigating detectors based on intersubband transitions in a quantum dots-in-a-well (DWELL) design. While exact material compositions and design for the various layers differs from group to group, the over all design remains constant. Our most basic design consists has the InAs dots are placed in an $\text{In}_{0.15}\text{Ga}_{0.85}\text{As}$ well, which in turn is positioned in a GaAs matrix. The DWELL detector is a hybrid design between a conventional QWIP and the QDIP and benefits from the advantages of both of its progenitors. Apart from sensitivity to normally incident light and lower dark currents, the DWELL structure demonstrates a better control over the operating wavelength and nature of the transition (bound-to-bound versus bound-to-continuum) ^[27]. In the DWELL structure an intersubband transition occurs when the electrons in the ground state of the QD are photoexcited into a bound state of the QW. The modeling of this structure and its excitations, however, is extremely challenging due to the nature of the potential profile. Previously, we have published some preliminary calculations of the electronic states and wavefunctions in the DWELL structure, and have obtained reasonably good agreement between the calculated energy level spacings and the obtained intersubband spectrum ^[26]. Based on a semiempirical estimate, we believe that the energy difference between the ground state in the dot and the conduction band edge of GaAs is around 250 meV ^[27]. In this paper, we wish to highlight some of the recent results that have been obtained using these DWELL detectors in focal plane arrays (FPAs). In Section 2, the growth and fabrication of the DWELL detectors and DWELL FPAs are discussed. Section 3 is devoted to the figures of merit for DWELL FPAs. Section 4 discusses recent advances, while Section 5 will conclude with upcoming advancements for DWELLs.

2. GROWTH AND FABRICATION OF DWELL FOCAL PLANE ARRAYS

For the purposes of this section we will detail the growth and fabrication of the basic DWELL structure mentioned above. Other structures grown and fabricated by our research group and others will be discussed in later sections.

2.1 Growth

The DWELL structures were grown in a V-80 molecular beam epitaxy system, with an As_2 cracker source. 2.4 monolayers (MLs) of InAs dots were deposited on the sample, at a rate of 0.053MLs^{-1} . The dots were Si-doped at a level of $1\text{e}^-/\text{QD}$. The cross-section of the device shown in Figure 1 consists of a 15-stack DWELL heterostructure between two n+ doped GaAs contact layers. The DWELL active regions are typically grown at 470°C , while the GaAs barrier was grown at a temperature of 590°C .

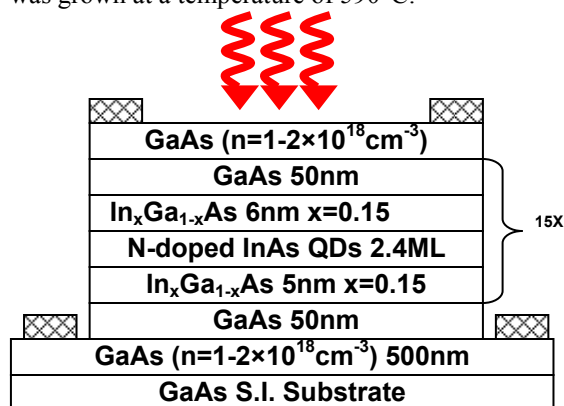


Figure 1: Diagram of the InAs/InGaAs DWELL after single pixel processing. Here the contact layers are show with ohmic-contacts. Between the contact layers lies the active region consisting of repetitions of quantum dots in quantum wells, nested in barriers. In this case, the detector is shown as being front illuminated.

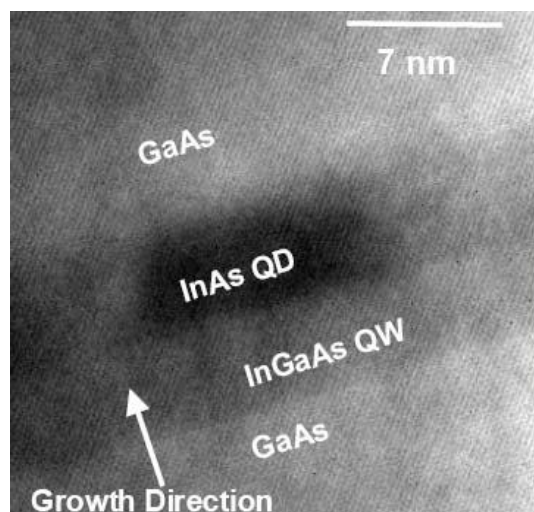


Figure 2: Cross-sectional TEM image of an InAs/InGaAs DWELL heterostructure.

The absence of threading dislocations in the heterostructures has been confirmed by cross-sectional transmission electron microscopy (TEM) [1]. High-resolution TEM images reveal that the dot is confined to the top half of the well (Figure 2). Room-temperature photoluminescence measurements on these samples with a 2.5mW, 632.8 nm He–Ne laser and a Ge detector yielded a peak at $\lambda = 1.22\text{--}1.24\mu\text{m}$, which is attributed to the interband ground state transition in the dot. Following the analysis by Kim et al [28] and using a 60:40 rule (conduction band : valence band ratio), we can attribute any peaks longer than $5.5\mu\text{m}$ observed in the photocurrent spectrum to a transition from the ground state in the dot to a bound state in the InGaAs well. By increasing the InGaAs well width, the position of the bound state in the well could be lowered. This effect would be expected to result in a red shift in the operating wavelength of the detector.

2.2 Fabrication

Post-growth processing was done using standard contact lithography, plasma-etching and metallization techniques, in a class 100 clean-room environment. Individual $400\mu\text{m}$ square n-i-n mesas with top pixel apertures, ranging from 25 to $300\mu\text{m}$ in diameter, were lithographically defined in the top metal contact for illumination in a front-normal configuration [1]. The contacts were annealed at 400°C using rapid thermal annealing.

The sample used to create the DWELL FPA was grown by MBE using the already proven single pixel DWELL structure (see Figure 1). In the structure used to create the FPA, the active regions of each pixel consisted of fifteen layers of InAs quantum dots embedded in $\text{In}_{0.15}\text{Ga}_{0.85}\text{As}$ quantum wells. The pixels are essentially identical to the single pixel structure shown in Figure 1 above, except that the substrate and bottom GaAs layer are removed and the pixel is flipped by 180° . Following the growth process, the sample was processed into a 320×256 array of detectors using standard lithography (each pixel occupies an area of approximately $5.76 \times 10^{-6}\text{cm}^2$, or $576\mu\text{m}^2$, and has a $25\mu\text{m}$ pitch). Processing included under bump metallization (UBM) and adding indium bumps at each detector location to facilitate device hybridization to a readout circuit, see Figure 3 & 4.

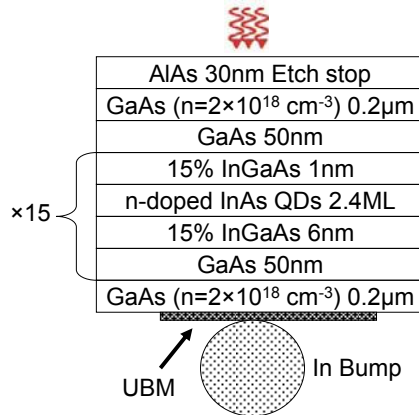


Figure 3: Schematic of a DWELL FPA pixel. After hybridization for a commercial read-out integrated circuit (ROIC) the substrate is removed and the FPA detector is back-illuminated.

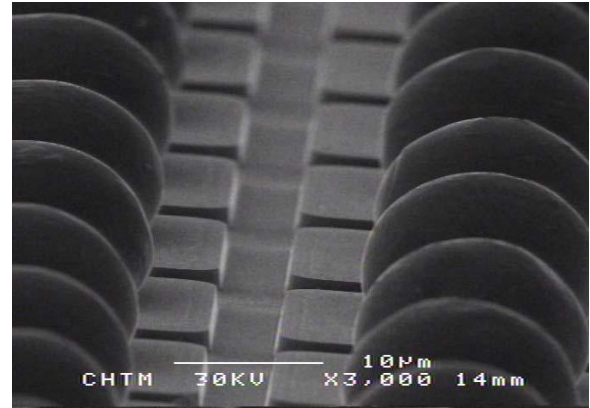


Figure 4 shows an SEM image of the DWELL FPA with indium bumps attached. The detector array was hybridized to a commercially available Indigo Systems Corporation ISC9705 readout integrated circuit (ROIC) by QmagiQ, Inc. to produce a usable FPA.

3. BROADBAND FIGURES OF MERIT

While most DWELLs presently being produced exhibit multi-color response it is still valuable to discuss the broadband, unfiltered, figures of merit for a DWELL FPA. Throughout this section we will discuss these broadband figures of merit by examining how they are derived and detailing new data for the 320×256 DWELL FPA detailed in the previous section. Several detector figures of merit can be calculated by measuring mean FPA output and noise versus irradiance. As a standard procedure, the irradiance is provided by a operating a calibrated black body source at various temperatures. Assuming a properly designed experimental set-up the irradiance values (E_q [photons/sec- cm^2] and E_e [Watts/ cm^2]) at the FPA can be treated as uniform across the array and were calculated using Equations 1 through 4 [29].

$$E_q = \frac{\pi L_q}{4(f\#)^2 + 1} \quad \text{Equation 1}$$

where L_q is photon radiance [photons/ $\text{cm}^2\text{-sec-sr-}\mu\text{m}$] and $f\#$ is the ratio of the lens focal length to the lens diameter,

which is a conveniently defined parameter,

$$L_q = \frac{2c}{\lambda^4 \left(\exp\left(\frac{hc}{\lambda kT}\right) - 1 \right)} \quad \text{Equation 2}$$

where h is Planck's constant [6.626×10^{-34} J-s], c is the speed of light [2.998×10^8 m/s], k is Boltzmann's constant [1.381×10^{-23} J/K], T is temperature [K],

$$E_e = \frac{\pi L_e}{4(f\#)^2 + 1} \quad \text{Equation 3}$$

L_e is photon radiance [Watts/(cm²-sr-μm)],

$$L_e = \frac{2hc^2}{\lambda^5 \left(\exp\left(\frac{hc}{\lambda kT}\right) - 1 \right)} \quad \text{Equation 4}$$

In general, up to the limit of the ROIC's integration capacitors, the DWELL FPA's output usually has a fairly linear response as a function of irradiance. For our running example of the detector detailed in the previous section we tested the FPA at detector biases of ($V_{DB} \sim 0.5, 0.75, 1.0$ and 1.1 V). Shown below in Figure 5, the ROIC integration capacitors were full at approximately -0.35 volts. Once this output voltage was reached, no further FPA response could be measured.

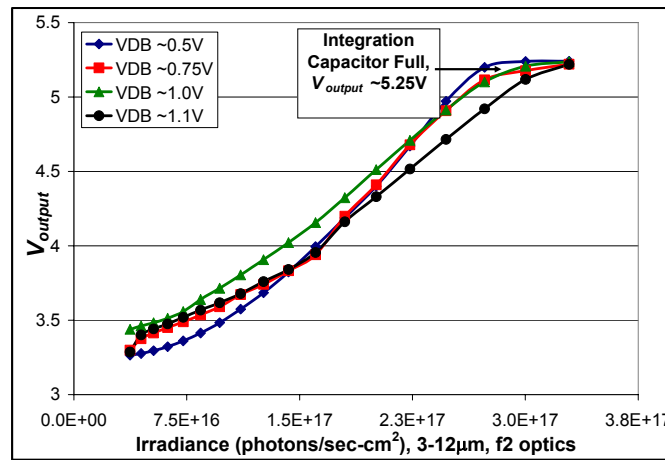


Figure 5: Output Voltage versus Irradiance for the DWELL FPA at 77K

When the detector array is operated in a photon shot noise dominant regime, the voltage output of DWELL FPA (V_{output}) along with the photon noise voltage (in Equation 5) can be utilized to calculate the conversion gain product, $C_G G$.

$$V_{nPhoton} = C_G G \sqrt{2\eta E_q A_d T_{int}} \quad \text{Equation 5}$$

where C_G is conversion gain (volts per electron), G is photoconductive gain, η is detector quantum efficiency (electrons per photon), E_q is photon irradiance [photons/sec-cm²], A_d is detector area [cm²], and T_{int} is integration time [s].

Squaring Equation 5 yields noise variance which can be used to solve for $\eta G E_q A_d T_{int}$. Next, this quantity can be substituted in Equation 6,

$$V_{output} = C_G \left(\eta G E_q A_d T_{int} + \frac{I_{dark} T_{int}}{q} \right) \quad \text{Equation 6}$$

where C_G is conversion gain, η is detector quantum efficiency [electrons per photon], G is photoconductive gain, E_q is photon irradiance [photons/sec-cm²], A_d is detector area [cm²], T_{int} is integration time [sec], I_{dark} is detector dark current [amps] and q is electron charge [1.6×10^{-19} Coulombs]. The slope of the resulting equation given by Equation 7,

$$V_{nPhoton}^2 = 2C_G G(V_{output}) - 2C_G^2 G \frac{I_{dark} T_{int}}{q} \quad \text{Equation 7}$$

corresponds to the $C_G G$ product. This method provides an estimate of the conversion-gain product at the four test biases. For most DWELL arrays there is an anticipated trend of higher $C_G G$ at higher biases (from the contribution of G)^[30]. For our example FPA, the estimated $C_G G$ product values for the four detector test biases are shown in Table 1.

V_{DETCOM} [V]	$C_G G$ [V/e ⁻]
5.5	1.30×10^{-6}
5.75	2.29×10^{-6}
6.0	2.13×10^{-6}
6.1	1.98×10^{-6}

Table 1: Conversion gain product ($C_G G$) estimates at 77K

3.1 Responsivity

Responsivity is defined as the detector output per unit of radiant input. A higher responsivity is generally desirable, since it is directly related to the sensitivity of the device and is proportional to the detector's quantum efficiency (QE). For a DWELL FPA, responsivity is proportional to the QE, photoconductive gain (G), and conversion gain (C_G) product. For the DWELL FPA shown in Figure 5, the responsivity was measured at four detector biases ($V_{DB} \sim 0.5, 0.75, 1.0$, and 1.1 volts) by measuring the output voltage versus irradiance. With this data the peak responsivities can be calculated by using the two equations below:

$$R_v \left[\frac{V}{\text{photon}} \right] = \frac{V_{output}}{\sum_{\lambda_1}^{\lambda_2} R_n(\lambda) E_e(\lambda, T) \tau_{win} d\lambda} \quad \text{Equation 8}$$

$$R_v \left[\frac{V}{W} \right] = \frac{V_{output}}{\sum_{\lambda_1}^{\lambda_2} R_n(\lambda) E_e(\lambda, T) \tau_{win} d\lambda} \quad \text{Equation 9}$$

where V_{output} is the output voltage [V], R_n is normalized spectral response, E_q is photon irradiance [photons/sec-cm²], E_e is irradiance [Watts/cm²], and $d\lambda$ is wavelength scanning step size from spectral response data [100nm]. To complete the peak responsivity calculations the collected spectral response data for the FPA must be used. Table 2 details the responsivity values for our example device at 77K.

V_{DB} [V]	R_v [V/photon]	R_v [V/W]
0.5	5.11×10^{-10}	4.32×10^7
0.75	1.24×10^{-9}	4.70×10^7
1.0	3.81×10^{-9}	3.16×10^7
1.1	8.33×10^{-9}	6.05×10^7

Table 2: Responsivity values at 77K

3.2 Noise Equivalent Power

Noise equivalent power (NEP) is a parameter defined as the required optical power incident on a photodetector that produces a signal-to-noise ratio equal to 1. This represents the minimum amount of optical input power that must be exceeded for detection to occur. A low value of NEP is an indicator of good detector performance, indicating a small amount of optical input is detectable. DWELL FPA NEP was calculated using calculated responsivity and Equation 10 [29],

$$NEP = \frac{V_n}{R_v} \quad \text{Equation 10}$$

where V_n is recorded noise voltage [VRMS] and R_v is voltage responsivity [V/W]. The NEP for our example is plotted against irradiance in Figure 6 and the minimum NEP values at each detector test bias are shown in Table 3.

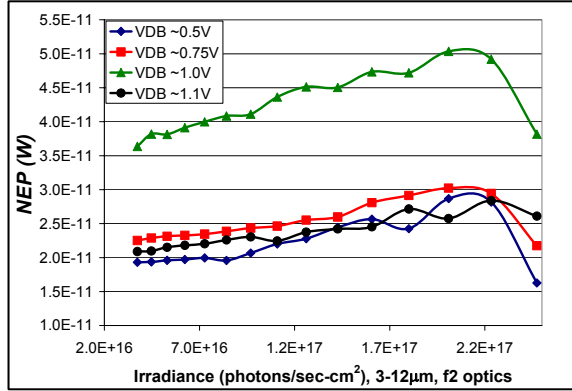


Figure 6: NEP versus Irradiance at 77K

V_{DB} [V]	NEP [W]
0.5	1.62×10^{-11}
0.75	2.17×10^{-11}
1.0	3.64×10^{-11}
1.1	2.09×10^{-11}

Table3: Minimum recorded NEP results at 77K

3.3 Noise Equivalent Irradiance

While noise equivalent irradiance (NEI) is simply a shift in units from NEP, it can be useful as a design property. NEI is defined by the number of photons per unit area incident upon a photodetector that produce a signal-to-noise ratio equal to 1 and, therefore, delineates the minimum flux detectable for the device. NEI is calculated with Equation 11,

$$NEI = \frac{V_n}{R_v A_d} \quad \text{Equation 11}$$

where V_n is recorded noise voltage [V_{RMS}], R_v is voltage responsivity [V/photon] and A_d is detector area [cm^2]. It should be noted that there is another definition of NEI that defined as the irradiance at an f1 input, rather than at the detector. Figure 7 shows an example of NEI plotted versus detector irradiance for the four test biases on the same FPA as depicted in Figures 5 and 6. Minimum NEI values for our example device are listed in Table 4.

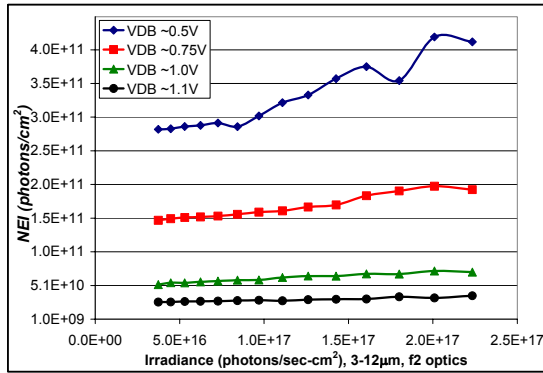


Figure 7: NEI versus Irradiance at 77K

V_{DB} [V]	NEI [photons/ cm^2]
0.5	2.83×10^{11}
0.75	1.48×10^{11}
1.0	5.24×10^{10}
1.1	2.64×10^{10}

Table 4: Minimum recorded NEI results at 77K

3.4 Detectivity

Inversely proportional to the NEP of a detector is the detectivity, or D^* , (units of $cm \cdot (Hz)^{1/2} / W$). As the name implies the detectivity is a measure of how little optical irradiance the FPA can detect and, therefore, having a high detectivity is important. The detectivity for a DWELL FPA is calculated using the NEP calculation results and Equation 12 [32] and Equation 13 [29],

$$\Delta f = \frac{1}{2T_{int}} \quad \text{Equation 12}$$

where T_{int} is ROIC integration time [sec], and

$$D^* = \frac{\sqrt{A_d \Delta f}}{NEP} \quad \text{Equation 13}$$

in which A_d is detector area [cm^2], and Δf is the noise bandwidth [Hz]. Detectivities for the same device detailed in the

figures and tables above are shown in the figure and table below.

V_{DB} [V]	D^* [cmHz ^{1/2} /W]
0.5	1.81×10^9
0.75	2.37×10^9
1.0	3.11×10^9
1.1	6.25×10^9

Table 5: Peak detectivity results at 77K

Under the conditions where photon noise dominates (BLIP), the theoretical BLIP detectivity may be used to estimate the QE of a photodetector. Theoretical BLIP detectivity is calculated by Equation 14 [29],

$$D^*_{BLIP} = \frac{\lambda}{2hc} \sqrt{\frac{\eta}{E_q}} \quad \text{Equation 14}$$

where λ is the wavelength [μm], h is Planck's constant [$6.626 \times 10^{-34} \text{ J}\cdot\text{s}$], c is the speed of light [$2.998 \times 10^8 \text{ m/s}$], η is detector quantum efficiency [electrons per photon] and E_q is photon irradiance [photons/sec-cm²]. The BLIP detectivity estimate was made using Equation 14 plotted against irradiance at two different values of QE. This plot is compared to the DWELL FPA detectivity values for $V_{DB} \sim 0.5\text{V}$ in Figure 9. Using this estimation technique, the quantum efficiency for DWELL FPA detailed in these figures is approximately 0.25 to 0.45% at 77K.

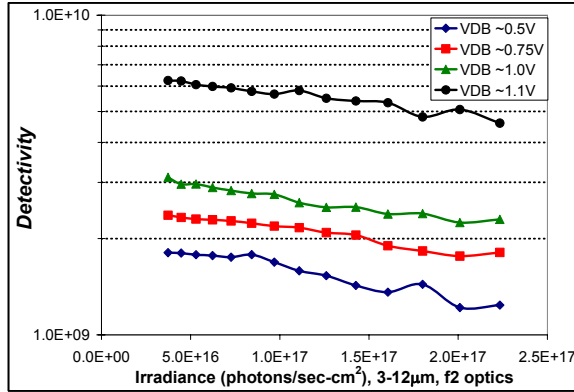


Figure 8: Detectivity versus Irradiance at 77K

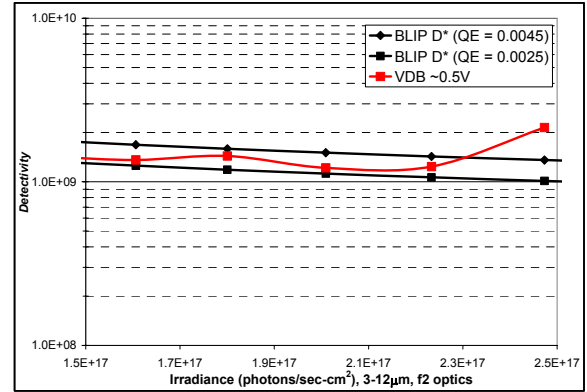


Figure 9: BLIP Detectivity for QE Estimation at 77K.

3.5 Noise Equivalent Difference in Temperature

The smallest difference in a uniform temperature scene that the FPA can detect is called the noise equivalent difference in temperature (NEDT, units of Kelvin). The smaller NEDT, therefore, the better, since it is a performance measure of the FPA's sensitivity. NEDT is calculated using the voltage output and noise versus irradiance data using the expression below [4]:

$$NEDT = \frac{\Delta T}{V_s / V_n} \quad \text{Equation 15}$$

where ΔT is the difference in black body temperatures [K], V_s is the response between two temperatures [V] and V_n is recorded noise voltage at the lower temperature [V]. Minimum NEDT values are observed just prior to the integration capacitor becoming full, where noise decreased due to a decline in readout noise. An example NEDT is plotted versus detector output in Figure 10 for the same device as the previous figures.

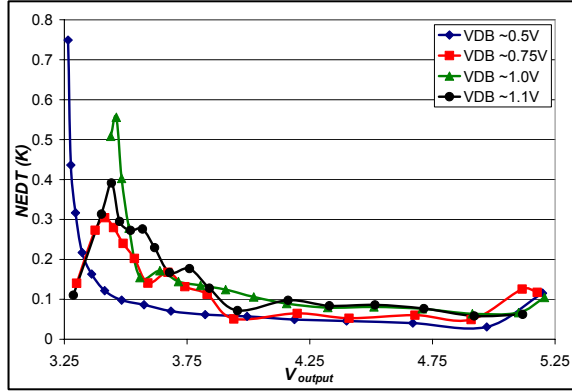


Figure 10: NEDT versus FPA Output Voltage at 77K

V_{DB} [V]	NEDT [K]
0.5	0.031
0.75	0.049
1.0	0.064
1.1	0.058

Table 6: Minimum NEDT results at 77K

4. RECENT ADVANCES IN DWELL FPAS

While the most groups have been focused primarily on monochromatic response for their DWELL FPAs, our group at UNM has been focused on bringing color to the infrared spectrum. Most of our designs, therefore, have two strong responses, one in the MWIR and one in the LWIR. This single bump, multicolor, technique provides enhanced utility for the detector in the applications mentioned in the introduction. For example, being able to examine a scene at two wavelengths removes the ambiguity generated by objects having different emissivity. This ability to differentiate objects is also the beginning of spectroscopy, enabling the fine differentiation between chemicals, biological agents, or types of tissues for medical and security applications^[31].

Using the example DWELL design detailed in the earlier section on broad band response, we have had a great deal of success in eliciting a two color response. For this FPA, standard processing was performed, ending with a single indium bump per pixel on the 320×256 array at UNM. The detector matrix was then hybridized by a commercial partner (QmagiQ LLC) to an Indigo Systems Corporation ISC9705 readout circuit. After hybridization, the FPA was tested at UNM using CamIRa™ system manufactured by SE-IR Corp. We observed two-color (MWIR and LWIR) response from the DWELL FPA at 77 K at a nominal bias voltage ranging from 0.5–1.0 V. Larger bias voltages could not be applied due to the saturation of the integration capacitors. The operation of the FPA was evaluated^[32].

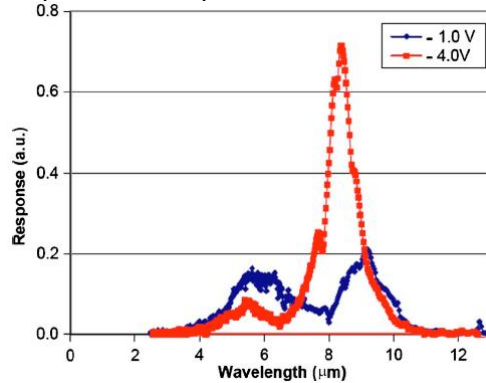


Figure 11: Multicolor response from a typical DWELL detector. The MWIR and LWIR peaks are probably from transitions from a state in the quantum dot to a state in the well and to the continuum, respectively. (note that ~1.0 data scaled by a factor of 5 for readability) [32].

The response of the detector existed in two bands. In each of the two bands, ASIO filter lenses were used to spectrally limit the incoming irradiance to 3–5 μm (f2) and 8–12 μm (f2.3), MWIR and LWIR, respectively. At a detector bias of 0.5 V, the integration time for DWELL FPA was 2.37 ms for the MWIR and LWIR responses. All measurements were made at a device temperature of 77 K with a liquid nitrogen pour fill Dewar to exclude noise caused by the compressor on a temperature controllable closed cycle Dewar^[32].

Figure 12 displays the detectivity results for the DWELL FPA. Peak values of 1.46×10^9 (cm^2Hz)^{1/2}/W and 3.64×10^{10} (cm^2Hz)^{1/2}/W (MWIR and LWIR, respectively) occurred just before the integration capacitors were fully charged. The

observed greater detectivity for the LWIR response compared to the MWIR response may be more artifact than fact: this is because LWIR could not be accurately measured in a single pixel at this low bias thus leading to an overestimate of the responsivity. In order to more accurately calculate the figures of merit, spectral response data for the DWELL FPA itself are needed. For this reason, we have ongoing work to establish the capability to perform spectral response measurements for an entire array [32].

In addition to responsivity and detectivity, we also calculated two-color noise equivalent difference in temperature (NEDT) for the DWELL FPA. This was accomplished by using the output voltage (V_o), noise voltage (v_n), and temperature step of the blackbody source (ΔT). Minimum NEDT values of 55 mK (MWIR) and 70 mK (LWIR) were measured for the DWELL FPA, Figure 13 [32].

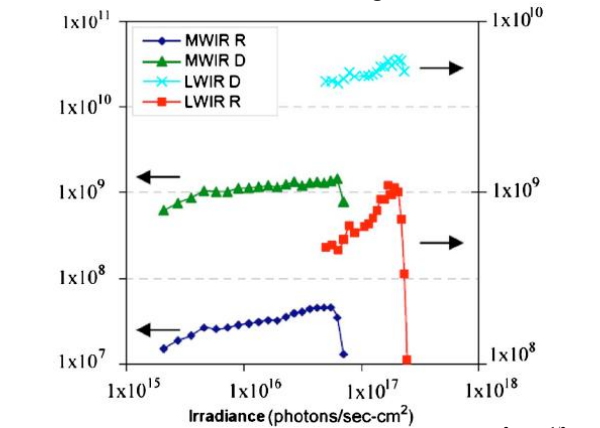


Figure 12: Peak responsivity (V/W) and detectivity [(cm² Hz)^{1/2}/W] for the MWIR (left axis) and LWIR (right axis) for the DWELL FPA at 77 K. Irradiance levels for MWIR and LWIR are 3–5 μm (f2) and 8–12 μm (f2.3), respectively [32].

V _{DB} [V]	R _v [V/photon]	R _v [V/W]	NEP [W]
MWIR			
0.5	1.39×10 ⁻⁹	6.76×10 ⁷	1.47×10 ⁻¹¹
0.75	2.08×10 ⁻⁸	4.68×10 ⁸	2.37×10 ⁻¹²
1.0	9.44×10 ⁻⁹	4.49×10 ⁷	2.63×10 ⁻¹¹
1.1	4.17×10 ⁻⁸	1.54×10 ⁸	7.90×10 ⁻¹²
LWIR			
0.5	6.30×10 ⁻¹⁰	7.30×10 ⁷	1.07×10 ⁻¹¹
0.75	1.88×10 ⁻⁹	9.35×10 ⁷	1.47×10 ⁻¹¹
1.0	4.77×10 ⁻⁹	5.28×10 ⁷	2.56×10 ⁻¹¹
1.1	8.48×10 ⁻⁹	7.04×10 ⁷	1.68×10 ⁻¹¹

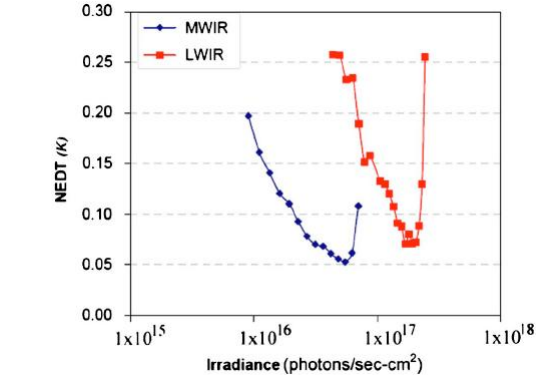


Figure 13: Noise equivalent temperature difference obtained in the MWIR and LWIR bands at 77 K. Irradiance levels for MWIR and LWIR are 3–5 μm (f2) and 8–12 μm (f2.3), respectively [32].

V _{DB} [V]	NEI [photons/cm²]	D* [cmHz ^{1/2} /W]	NEDT [K]
MWIR			
0.5	1.30×10 ¹¹	2.38×10 ⁹	1.88×10 ⁹
0.75	9.23×10 ⁹	2.54×10 ¹⁰	3.57×10 ⁹
1.0	2.18×10 ¹⁰	4.30×10 ⁹	3.72×10 ⁹
1.1	5.09×10 ⁹	1.65×10 ¹⁰	5.18×10 ⁹
LWIR			
0.5	1.17×10 ¹¹	6.12×10 ⁹	1.95×10 ⁹
0.75	1.27×10 ¹¹	3.63×10 ⁹	1.73×10 ⁹
1.0	4.93×10 ¹⁰	4.41×10 ⁹	2.65×10 ⁹
1.1	2.49×10 ¹⁰	7.76×10 ⁹	3.62×10 ⁹

Tables 7 & 8: Summary of two-color figures of merit.

By reviewing the two-color response performance measures, one can see that the figures of merit calculated tend to be better in the MWIR region, though the difference between MWIR performance and LWIR performance was not dramatically different at the four detector biases used in testing. This is attributed to the fact that the MWIR and LWIR responses are comparable at these lower detector biases, where bound-to-continuum energy transitions are favored leading to a slightly larger MWIR response. At larger reverse bias the LWIR response would be expected to become dominant because the probability of carriers tunneling from the bound-to-bound and bound-to-quasi-bound states increases, leading to the increased LWIR response. With the 9705 ROIC two-color response is noted from the measured spectral response of the FPA, but because of the limitation of biases that can be applied with the 9705, the concept of a bias tunable FPA camera could not be more thoroughly explored.

5. FUTURE ADVANCEMENTS & CONCLUSION

The purpose of this article is to give an overview of the important figures of merit for DWELL FPAs and review the recent advancements in field. There are a number of new and exciting techniques that are starting to appear in single pixel devices that will soon be applied to FPAs as well. One of these advancements includes a new DWELL design that uses a double-well. In this structure the GaAs barriers are replaced with AlGaAs barriers and the role of the primary well is played by a GaAs layer. Here, the InGaAs layer thicknesses, which constitute the second well, are reduced to a minimum and, therefore, the strain due to lattice mismatch with the GaAs substrate is also minimized. This enables larger stacks to be grown (30-80 repetitions of the active region). FPAs of this design are presently under test at CHTM at the time of this article being written [42, 43].

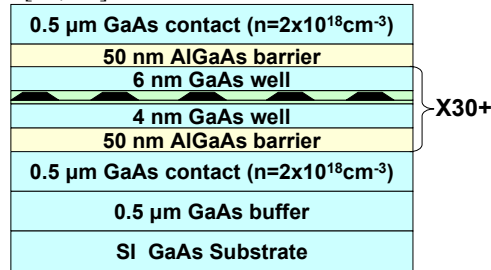


Figure 14: A schematic for the structure of a low-strain DWELL, specifically a double DWELL or a DDWELL design. Here, a GaAs well acts as a primary well, surrounded by AlGaAs barriers. Inside the GaAs well, lies a minimized InGaAs well surrounding the InAs QDs [33 & 34].

Based on a semi-empirical estimate, we believe that the energy difference between the ground state in the dot and the conduction band edge of GaAs is around 164 meV [27]. We have modeled the electronic states and wavefunctions in the DWELL structure, using Bessel function expansion [26] and using Finite Difference Method, Figure 15. There is a reasonably good agreement between the calculated energy level spacings and the obtained intersubband spectrum, Table 9.

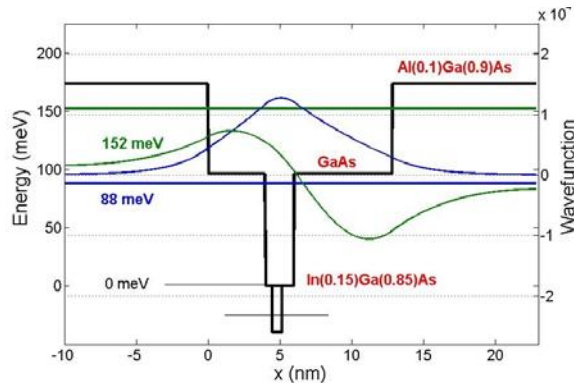


Figure 15: Model of the double-DWELL photodetectors active region. Note: the portion of the band diagram corresponding to the InAs QD is not depicted here. The ground state and first excited state calculated are solely for the nested QW system. The two modeled states show a close match with the observed transition wavelengths observed.

	Measured	Calculated
MWIR	5.5 μm	8.3 μm
LWIR	5.6 μm	7.9 μm

Table 9: Comparison between the measured peak values for the double-DWELL photo detectors and the FDM calculated values.

The results confirm that the LWIR response is due to transition from ground state of the quantum dot to ground state of the quantum well structure while the MWIR response is from the transition to second bound state, which is very close to the continuum state. From this modeling, the strong quantum confined stark effect in asymmetric quantum dots is apparent, which produces a shift of $\sim 2\text{mm}$ in the LWIR response for change in the bias polarity. This effect is useful for tunable response from the DWELL detectors.

Another advancement uses a resonant cavity to increase the number of passes incident photons make through the active region and, therefore, enhance the quantum efficiency^[35]. The resonant cavity (RC) is formed using a DBR at the bottom of the stack; the natural semiconductor-air interface is all that is used at the top for this design, Figure 16.

This RC-DWELL was designed to enhance the LWIR signal, which does enhance by approximately a factor of 3, Figure 17^[35].

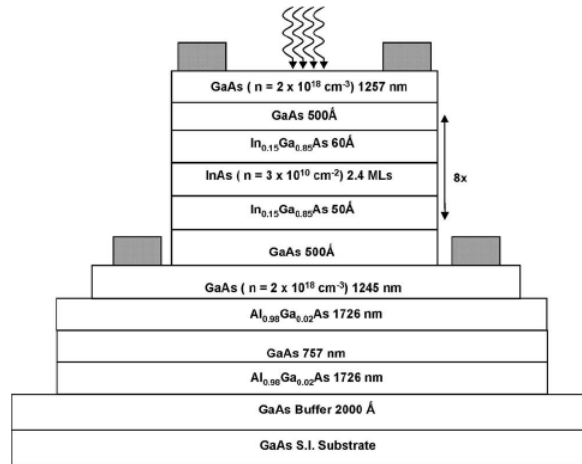


Figure 16: A schematic of the structure for a processed resonant cavity (RC) DWELL, by adding the DBR at the bottom of the stack the incident light will make multiple passes through the active region enhancing QE.^[35]

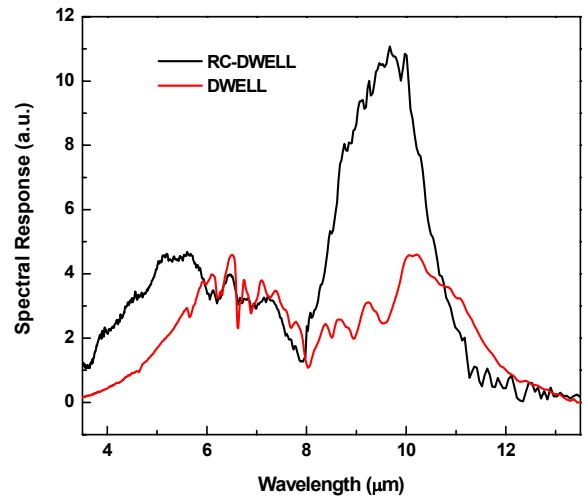


Figure 17: Spectral response data for the RC-DWELL (upper curve) and the standard DWELL (lower curve) samples. All the spectra were taken at T=30 K at a bias of $V_b = -1.8$ V^[35].

Additional experiments are also being performed to enhance the DWELLs functionality, from surface plasmons and phonic crystals as part of the detectors^[36] to specialized capping materials for the quantum dots to enhance their functionality directly^[37]. In the end, DWELLs are a young technology and their application in FPAs is even more recent. In the coming years of research one can expect significant improvement in a number of areas: operating temperature, sensitivity (NEDT), QE, and functionality (multicolor).

ACKNOWLEDGMENTS

The authors would like to acknowledge the work and efforts of all of their colleagues whom have made this work possible, including: Dr. A. Stintz, Dr. A. Amtout, Dr. P. Dowd, G. von Winckel, R. S. Attaluri, S. Annamalai, N. R. Weisse-Bernstein, D. Formann, S. Raghavan, S. J. Lee, and J. S. Brown. Work supported by grants from Air Force Office of Scientific Research (AFOSR), Air Force Research Laboratory (AFRL) and National Science Foundation (NSF).

REFERENCES

- [1] Raghavan S, Rotella P, Stintz A, Fuchs B, Krishna S, Morath C, Cardimona D A and Kennerly S W 2002 Appl. Phys. Lett. 81 1369 and references therein
- [2] Maimon S, Finkman E, Bahir G, Schacham S E, Garcia J M and Petroff P M 1998 Appl. Phys. Lett. 73 2003
- [3] Chen Z, Baklenov O, Kim E T, Mukhametzhanov I, Tie J and Madhukar A 2001 J. Appl. Phys. 89 4558
- [4] Stiff-Roberts A D, Krishna S, Bhattacharya P and Kennerly S 2002 J. Vac. Sci. Technol. B 20 1185
- [5] Wang S Y, Lin S D, Wu H W and Lee C P 2001 Appl. Phys. Lett. 78 1023
- [6] Liu H C, Gao M, McCaffrey J, Wasilewski Z R and Fafard S 2001 Appl. Phys. Lett. 78 79
- [7] Chu L, Zrenner A, Bohm G and Abstreiter G 1999 Appl. Phys. Lett. 75 3599
- [8] Rappaport N, Finkman E, Brunhes T, Boucaud P, Sauvage S, Yam N, Le Thanh V and Boucher D 2000 Appl. Phys. Lett. 77 3224
- [9] Jiang L, Li S S, Yeh N-T, Chyi J-I, Ross C E and Jones K S 2003 Appl. Phys. Lett. 82 1986
- [10] Phillips J 2002 J. Appl. Phys. 91 4590
- [11] Sidorov Yu G, Dvoretzky S A, Yakushev M V, Mikhailov N N, Varavin V S and Liberman V I 1997 Thin Solid Films 306 253

- [12] Motohisa, J., Kumakure, K., Kishida, M., Yamazaki, T., Fukui, T., Hasegawa, H., and Wada, K.: 'Fabrication of GaAs/AlGaAs quantum dots by metalorganic vapor phase epitaxy on patterned GaAs substrates', *Jpn. J. Appl. Phys.*, 1995, 34, pp. 1098–1101
- [13] Ryzhii, V.: 'Characteristics of quantum well infrared photodetectors', *J. Appl. Phys.*, 1997, 81, pp. 6442–6448
- [14] Shen, A., Liu, H.C., Buchanan, M., and Gao, M.: 'Progress on optimization of p-type GaAs/AlAs quantum well infrared photodetectors', *J. Vac. Sci. Technol. A*, 2000, 18, pp. 601–604
- [15] Horiguchi, N., et al.: 'Quantum dot infrared photodetector using modulation doped InAs self-assembled quantum dots', *Jpn. J. Appl. Phys.*, 1999, 38, pp. 2559–2561
- [16] Liu, H.C., Dudek, R., Shen, A., Dupont, E., Song, C.Y., Wasilewski, Z.R., and Buchanan, M.: 'High absorption (.90%) quantum-well infrared photodetectors', *Appl. Phys. Lett.*, 2001, 79, pp. 4237–4239
- [17] Zibik E A et al 2004 *Phys. Rev. B* 70 161305
- [18] Kim K, Urayama J, Norris T B, Singh J, Phillips J and Bhattacharya P 2002 *Appl. Phys. Lett.* 81 670
- [19] Philips J, Bhattacharya P, Kennerly S W, Beekman D W and Dutta M 1999 *IEEE J. Quantum Electron.* 35 936
- [20] Phillips, J., Bhattacharya, P., Kennerly, S.W., Beekman, D.W., and Dutta, M.: 'Self-assembled InAs-GaAs quantum-dot intersubband detectors', *IEEE J. Quantum Electron.*, 1999, 35, (6), pp. 936–943
- [21] Ryzhii, V., et al.: 'Dark current quantum dot infrared photodetectors', *Jpn. J. Appl. Phys.*, 2000, 39, L1283–L1285
- [22] Ryzhii, V.: 'The theory of quantum-dot infrared phototransistors', *Semicond. Sci. Technol.*, 1996, 11, pp. 759–765
- [23] El Mashade, M.B., Ashry, M., and Nasr, A.: 'Theoretical analysis of quantum dot infrared photodetectors', *J. Semicond. Sci. Technol.*, 2003, 18, pp. 891–900, <http://www.iop.org/EJ/abstract/0268-1242/18/9/314>.
- [24] A. Nasr and M.B. El Mashade "Theoretical comparison between quantum well and dot infrared photodetectors" *IEE Proc.-Optoelectron.*, Vol. 153, No. 4, August 2006
- [25] H. Lim, S. Tsao, W. Zhang, and M. Razeghi, High-performance InAs quantum-dot infrared photodetectors grown on InP substrate operating at room temperature, *APPLIED PHYSICS LETTERS* 90, 131112 (2007)
- [26] Amtout A, Raghavan S, Rotella P, von Winckel G, Stintz A and Krishna S 2004 *J. Appl. Phys.* 96 3782
- [27] Krishna S, Raghavan S, von Winckel G, Stintz A, Ariyawansa G, Matsik S G and Perera A G U 2003 *Appl. Phys. Lett.* 83 2745
- [28] Kim E-T, Chen Z and Madhukar A 2001 *Appl. Phys. Lett.* 79 3341
- [29] Dereniak, E. L. and Boreman, G., *Infrared Detectors and Systems*, (Wiley, New York, 1996)
- [30] Campbell, J and Madhukar, A., *Quantum Dot Infrared Photodetectors*,
- [31] S. Krishna, Quantum dots-in-a-well infrared photodetectors, *J. Phys. D: Appl. Phys.* 38 (2005) 2142–2150
- [32] E. Varley, M. Lenz, S. J. Lee, J. S. Brown, D. A. Ramirez, A. Stintz, and S. Krishna, Single bump, two-color quantum dot camera, *APPLIED PHYSICS LETTERS* 91, 081120 (2007)
- [33] R. V. Shenoi, R. S. Attaluri, J. Shao, Y.D. Sharma, A. Stintz, T. E. Vandervelde, and S. Krishna, Low Strain InAs/InGaAs/GaAs Quantum Dots-in-a-Well Infrared Photodetector, *JVSTB* In Press
- [34] R.S. Attaluri, R. Shenoi, J. Shao, T.E. Vandervelde, A. Stintz, and S. Krishna, Three-Color InAs/InGaAs/GaAs Dots-in-Double-Well (DDWELL) Infrared Photodetector, *Jour. Appl. Phys.* Submitted
- [35] R. S. Attaluri, J. Shao, K. T. Posani, S. J. Lee, J. S. Brown, A. Stintz, and S. Krishna, Resonant cavity enhanced InAs/ In_{0.15}Ga_{0.85}As dots-in-a-well quantum dot infrared photodetector, *J. Vac. Sci. Technol. B* 25 4., Jul/Aug 2007
- [36] R. V. Shenoi D. A. Ramirez, Y. Sharma, R. S. Attaluri, J. Rosenberg, O. J. Painter, and S. Krishna, "Plasmon Assisted Photonic Crystal Quantum Dot Sensors", *Nanophotonics and Macrophotonics for Space Environments*(6713) *SPIE Optics Photonics SanDiego*(2007)
- [37] T.E. Vandervelde, J. Shao, A. Stintz, and S. Krishna,, Investigation of Shape Engineering in InAs Quantum Dots Using Various Capping Materials, *MRS Fall Meeting 2007*, Boston, MA.